


Nanoconfinement facilitates reactions of carbon dioxide in supercritical water

Received: 31 March 2022

Nore Stolte ^{1,4}, Rui Hou ^{1,2} & Ding Pan ^{1,2,3} ✉

Accepted: 27 September 2022

Published online: 08 October 2022

 Check for updates

The reactions of CO₂ in water under extreme pressure-temperature conditions are of great importance to the carbon storage and transport below Earth's surface, which substantially affect the carbon budget in the atmosphere. Previous studies focus on the CO₂(aq) solutions in the bulk phase, but underground aqueous solutions are often confined to the nanoscale, and nanoconfinement and solid-liquid interfaces may substantially affect chemical speciation and reaction mechanisms, which are poorly known on the molecular scale. Here, we apply extensive *ab initio* molecular dynamics simulations to study aqueous carbon solutions nanoconfined by graphene and stishovite (SiO₂) at 10 GPa and 1000 ~ 1400 K. We find that CO₂(aq) reacts more in nanoconfinement than in bulk. The stishovite-water interface makes the solutions more acidic, which shifts the chemical equilibria, and the interface chemistry also significantly affects the reaction mechanisms. Our findings suggest that CO₂(aq) in deep Earth is more active than previously thought, and confining CO₂ and water in nanopores may enhance the efficiency of mineral carbonation.

Aqueous fluids play a critical role in transporting carbon between Earth's surface and interior¹⁻³, which is a substantial part of Earth's carbon cycle, with great implications for global climate and human energy consumption. It has long been assumed that aqueous carbon solutions under extreme pressure (P) and temperature (T) conditions are made by mixtures of neutral gas molecules⁴, e.g., H₂O, CO₂, CH₄; however, recent studies showed that important chemical reactions occur between water and carbon species, resulting in significant amounts of ionic products, which may further participate in water-rock interactions and the formation of diamonds in Earth's interior⁵⁻¹¹. Most of the previous studies focus on the properties of aqueous carbon solutions in the bulk phase. In fact, aqueous solutions in deep Earth are often confined to the nanoscale in pores, grain boundaries, and fractures of Earth's materials¹²⁻¹⁴, where the physical and chemical properties of solutions may be dramatically different from those of bulk solutions. In addition, in carbon capture and sequestration efforts, CO₂ mineralization occurring in water trapped in porous rocks offers an efficient and secure method to permanently store carbon

underground with a low risk of return to the atmosphere¹⁵. The behavior of aqueous carbon solutions under nanoconfinement at extreme P-T conditions is of great importance to the deep carbon cycle and CO₂ storage, but is poorly understood on the molecular scale.

Previous studies reported that nanoconfinement substantially affects properties of water, e.g., equation of state¹⁶⁻¹⁸, phase behavior¹⁹⁻²¹, dielectric constant²²⁻²⁶, and diffusion²⁷⁻²⁹, as a result, the reactivity of solutes under confinement may be very different from that in bulk solutions³⁰. The dimensional reduction and increased fluid density could enhance reactions between small solutes in nanoconfinement^{31,32}, whereas reactions involving large reactants or intermediates may be sterically hindered³³. Further, the increase of the dielectric constant of nanoconfined water parallel to the confining surface leads to the stabilization of aqueous reaction products with charges³³, causing the enhanced autodissociation of water²³. The solid-liquid interface also greatly affects the properties of confined aqueous solutions³⁴. Preferential adsorption of solutes at the confining interface may shift reaction equilibria. For example, in the production

¹Department of Physics, Hong Kong University of Science and Technology, Hong Kong, China. ²HKUST Shenzhen-Hong Kong Collaborative Innovation Research Institute, Shenzhen, China. ³Department of Chemistry, Hong Kong University of Science and Technology, Hong Kong, China. ⁴Present address: Lehrstuhl für Theoretische Chemie, Ruhr-Universität Bochum, 44780 Bochum, Germany. ✉ e-mail: dingpan@ust.hk

of methane from carbon dioxide at hydrothermal vent conditions ($\text{CO}_2 + 4 \text{H}_2 \rightleftharpoons \text{CH}_4 + 2 \text{H}_2\text{O}$), hydrophilic pore surfaces adsorb water, favoring the production of methane³⁵.

Nanoconfinement and interface chemistry may both likely change the properties of aqueous carbon solutions, but a molecular understanding is lacking on how chemical speciation and reaction mechanisms are affected. It was experimentally found that magnesite precipitates much faster in nanoscale water films than in bulk water³⁶. Because it is very challenging to study aqueous solutions under nanoconfinement in experiment, atomistic simulations are widely used. Many studies applied classical force fields^{27,29,34,37}, which were usually designed for bulk solutions at ambient conditions; their accuracy at extreme conditions is not well tested. As a comparison, *ab initio* molecular dynamics (AIMD) simulations do not rely on experimental input or empirical parameters^{38–40}. We solve the many-body electronic structure numerically, so the breaking and forming of chemical bonds, electronic polarizability, and charge transfer are all treated at the quantum mechanical level^{40,41}. The AIMD method is widely considered as one of the most reliable methods to make predictions, and many simulation results were later confirmed by experiments^{40,41}.

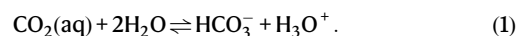
Here, we performed extensively long AIMD simulations to study $\text{CO}_2(\text{aq})$ solutions nanoconfined by graphene and stishovite (SiO_2) at 10 GPa and 1000–1400 K. These P-T conditions are typically found in Earth's upper mantle. We compared the $\text{CO}_2(\text{aq})$ reactions in nanoconfinement with those in the bulk solutions, and examined how weak and strong interactions between confining walls and confined solutions affect chemical speciation and reaction mechanisms. Although graphene is not found in deep Earth so far, it provides a good comparison with stishovite. In graphene confinement, there are no chemical reactions between graphene and solutions, whereas the dangling atoms in stishovite actively participate in aqueous carbon reactions, so we can compare the effects of spatial confinement with and without interface chemistry. What's more, thanks to the rapid development in the fabrication and characterization of 2D materials in recent years, experimentalists are now able to delicately measure the properties of aqueous solutions under graphene nanoconfinement³⁰, so we hope our study can also attract many follow-up experiments. Our work is relevant to the carbon transformation in deep Earth, and also helps us to understand atomistic mechanisms of CO_2 mineralization in the carbon capture and storage.

Results and discussion

Graphene nanoconfinement

We first studied $\text{CO}_2(\text{aq})$ solutions confined by two graphene sheets at -10 GPa, and 1000–1400 K (Fig. 1a). The graphene sheet separation was 9.0 and 9.2 Å at 1000 and 1400 K, respectively. We modeled the graphene sheets using a distance-dependent potential acting on the carbon and oxygen atoms, which was fitted to the interaction energies calculated using diffusion quantum Monte Carlo⁴² and van der Waals density functional theory⁴³ (see Supplementary Methods). We calculated the pressure of confined solutions parallel to the graphene sheets, which is -10 GPa (see Supplementary Methods). In addition, we also used atom number density profiles to calculate actual volumes that aqueous carbon solutions occupy, and then applied the equation of state of CO_2 and water mixtures to obtain the pressure⁴⁴.

We directly dissolved CO_2 molecules in the supercritical water, and the initial mole fraction of $\text{CO}_2(\text{aq})$ is 0.185. The CO_2 molecules reacted frequently with water, and we performed long AIMD simulations until the concentrations of carbon species reached equilibria (see Supplementary Fig. 3). Initially, the reaction between $\text{CO}_2(\text{aq})$ and H_2O produces bicarbonate ions (HCO_3^-):



This reaction in some cases occurs in one step, or involves the dissociation of water so that OH^- can react with $\text{CO}_2(\text{aq})$ to form HCO_3^- (aq). The generated bicarbonate ion may further accept a proton to become a carbonic acid molecule ($\text{H}_2\text{CO}_3(\text{aq})$), or may lose a proton to become a carbonate ion (CO_3^{2-} (aq)). The major carbon species in the solutions are $\text{CO}_2(\text{aq})$, CO_3^{2-} , HCO_3^- , and H_2CO_3 .

We compared the chemical speciation of the solutions under nanoconfinement and in the bulk phase at the same P-T conditions¹⁰. Figure 2 shows that at 1000 K, the mole percent of $\text{CO}_2(\text{aq})$ in total dissolved carbon under nanoconfinement is $1.3 \pm 0.9\%$, whereas it is $15.2 \pm 2.0\%$ in the bulk solution. The mole percent of HCO_3^- under nanoconfinement ($50.0 \pm 1.0\%$) is higher than that in the bulk solution ($35.9 \pm 0.7\%$), and the concentrations of $\text{H}_2\text{CO}_3(\text{aq})$ are similar ($42.7 \pm 1.7\%$ vs. $46.8 \pm 1.5\%$). With increasing temperature from 1000 K to 1400 K, the mole percents of $\text{CO}_2(\text{aq})$ under nanoconfinement and in the bulk solution increase to $14.5 \pm 3.2\%$ and $58.8 \pm 2.0\%$, respectively. The equilibrium concentrations of $\text{CO}_2(\text{aq})$ in the nanoconfined

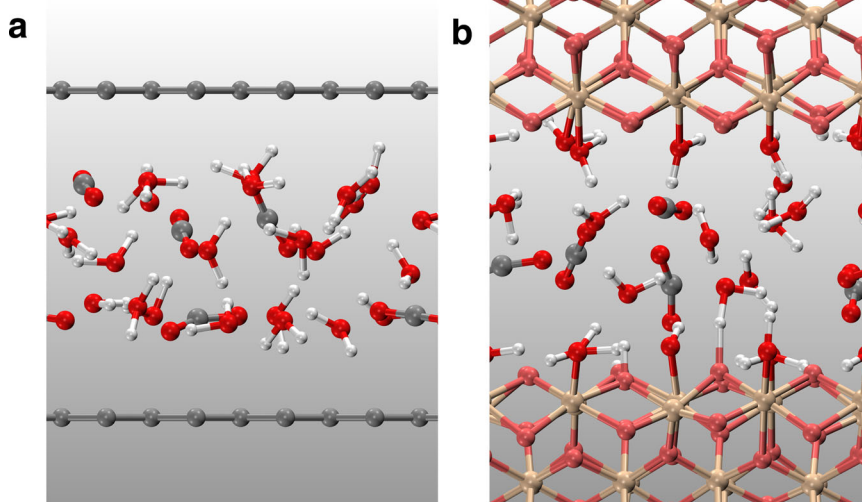


Fig. 1 | Snapshots of *ab initio* molecular dynamics simulations under confinement. **a** $\text{CO}_2(\text{aq})$ confined by graphene sheets. **b** CO_2 confined by cleaved stishovite (SiO_2) (100) slabs. Red balls represent oxygen atoms in solutions, and pink balls are

oxygen atoms in SiO_2 . Gray, white, and yellow balls are carbon, hydrogen, and silicon atoms, respectively.

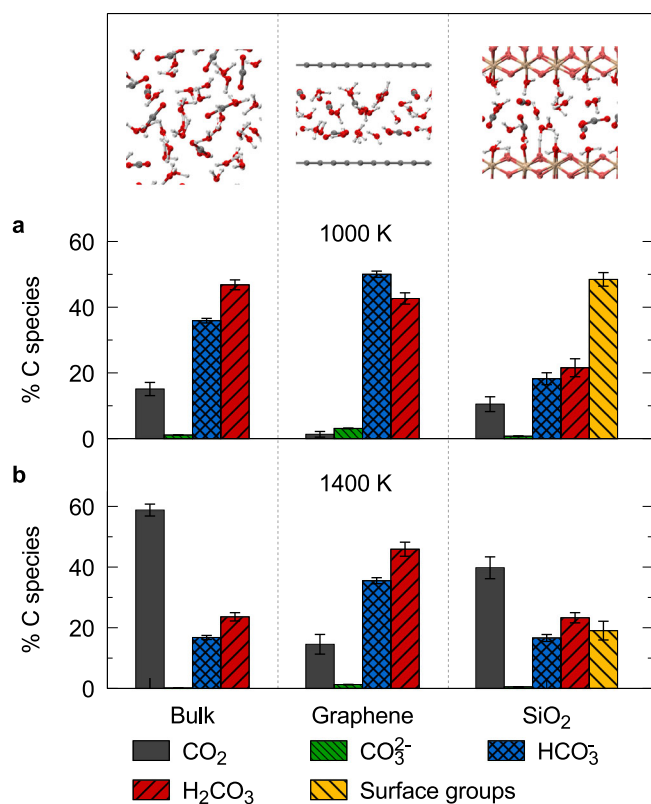


Fig. 2 | Mole percents of carbon species in the CO₂(aq) solutions in bulk and nanoconfined by graphene and stishovite (SiO₂) at chemical equilibria. The initial mole fraction of CO₂(aq) is 0.185. The pressure is -10 GPa. The temperatures are **a** 1000 K and **b** 1400 K. The data of bulk solutions in **(a)** are from ref. 10, and the bulk data in **(b)** were interpolated using the simulation results in ref. 10. Uncertainties were obtained using the blocking method⁶⁸.

solutions are lower than those in the bulk solutions at the two temperature conditions studied here, suggesting that nanoconfinement promotes the CO₂(aq) reactions. When increasing temperature along an isobar, due to thermal entropy effects, small molecules like CO₂(aq) are more favored. We did not see obvious difference in reaction rates between nanoconfined and bulk solutions.

To understand why nanoconfinement promotes CO₂(aq) reactions, we analyzed the water structure in Fig. 3. In the graphene-confined solutions, there are two sharp density peaks for oxygen atoms, corresponding to two water layers (Fig. 3a, b). We found that the carbon-containing ions and molecules in these two layers tend to align parallel to the graphene sheets (Fig. 4), and CO₂(aq) mostly reacts with water molecules in the same layer (Supplementary Figs. 6 and 7). Nanoconfinement increases the probability of reactive encounters between CO₂(aq) and solvent molecules, as diffusion is restricted to two dimensions³³. It has been reported that the dielectric constant of nanoconfined water in the direction parallel to the confining surfaces (ϵ_{\parallel}) increases significantly compared to the bulk value (ϵ_0). In water, the Coulomb interaction between two ions is $F = \frac{q_1 q_2}{\epsilon_0 r}$, where q_1 and q_2 are the charges of the two ions, and r is their distance. With increasing the dielectric constant, the magnitude of F decreases, so it is easier to separate a cation from an anion. Consistent with this, water molecules dissociate more easily under nanoconfinement^{23,25}. In CO₂(aq) solutions, the produced OH⁻ ions from the water self-ionization are subsequently available to react with CO₂(aq) (reaction (1)). The enhancement of ϵ_{\parallel} also further stabilizes HCO₃⁻ and CO₃²⁻ ions generated in the reaction between CO₂(aq) and H₂O or OH⁻. As a result, more CO₂(aq) molecules react under nanoconfinement than in bulk. When the interlayer distance between graphene sheets increases

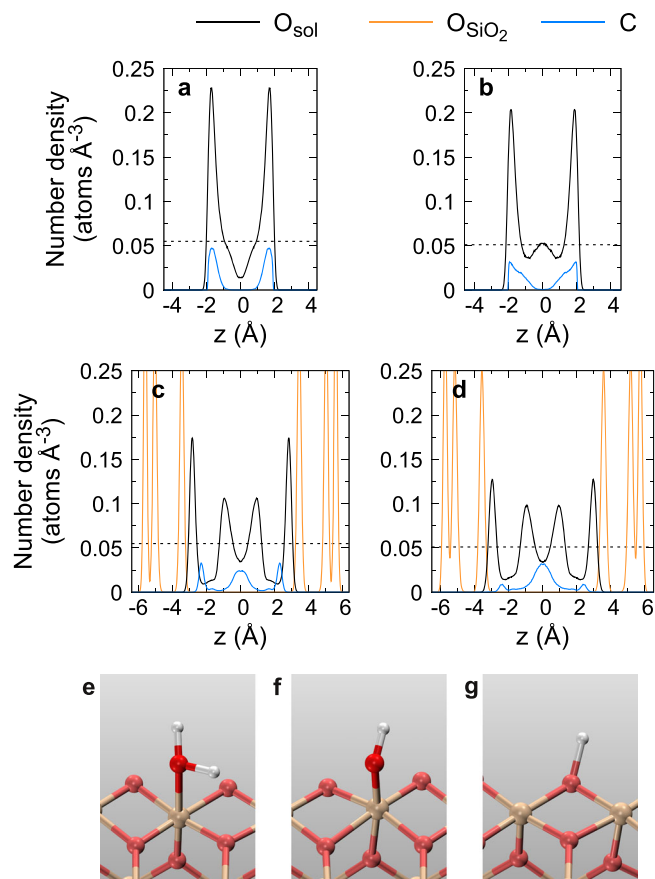


Fig. 3 | Number density profiles of oxygen atoms and carbon atoms along the z axis, normal to the confining surfaces. **a, b** The solutions under graphene confinement at 1000 and 1400 K, respectively. **c, d** The solutions under stishovite confinement at 1000 and 1400 K, respectively. O_{sol} refers to the oxygen atoms in solutions (black lines), O_{SiO₂} refers to the oxygen atoms in stishovite (orange lines), and C refers to carbon atoms (blue lines). The initial mole fraction of CO₂(aq) is 0.185. The pressure is -10 GPa. The center of confined fluids is set at $z = 0$, and the density distributions have been symmetrized. The horizontal black dashed lines represent the oxygen density in the bulk solutions at the corresponding P-T conditions⁴⁴. **e–g** The H₂O molecule, the OH⁻, and H⁺ ions bonded to the stishovite (100) surface, respectively.

beyond -1.5 nm, the bulk behavior of water is recovered in the center of the slit pore and the effects of nanoconfinement become less obvious²⁵.

Stishovite nanoconfinement

After studying the effects of graphene nanoconfinement, we turned to the confinement by a realistic mineral in deep Earth, stishovite, which is a stable phase of SiO₂ (space group: P4₂/mnm) at the P-T conditions studied here^{45,46} and a major component of subducted oceanic crust⁴⁷, playing a substantial role in transporting water into Earth's mantle⁴⁸. We exposed the cleaved stishovite (100) face, one of the low-energy surfaces⁴⁹, to the carbon solutions as shown in Fig. 1b. We carried out constant-pressure (NPT) simulations to keep the pressure perpendicular to the solid–liquid interface at -10 GPa, and then we found that the distance between the outermost oxygen atoms in two stishovite (100) surfaces is -7 Å (Supplementary Table 1). In deep Earth, aqueous solutions released from subducting materials in devolatilization processes tend to locate at grain boundaries¹⁴. The size of the pores at grain boundaries is typically between 0.4 and 1.2 nm¹³, and our confinement width is within this range.

Figure 2 shows the chemical speciation of aqueous carbon solutions under stishovite confinement at -10 GPa and 1000–1400 K. We

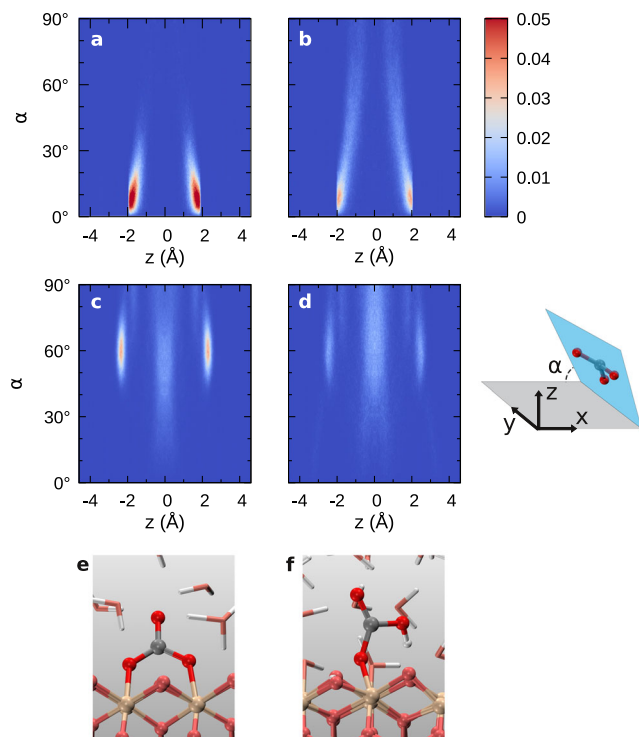


Fig. 4 | Orientation distribution of sp^2 carbon species in $CO_2(aq)$ solutions. The dihedral angle α is between the confinement interface and the plane defined by the three oxygen atoms in sp^2 carbon species. **a, b** The solutions under graphene confinement at 1000 and 1400 K, respectively. **c, d** The solutions under stishovite confinement at 1000 and 1400 K, respectively. The pressure in all solutions are -10 GPa. The initial mole fraction of $CO_2(aq)$ is 0.185. The center of confined fluids is set at $z = 0$, and the angle distributions have been symmetrized. **e, f** The CO_3^{2-} and HCO_3^- ions adsorbed on the stishovite (100) surface, respectively.

found that at chemical equilibrium, $48.5 \pm 2.1\%$ (1000 K) and $19.1 \pm 3.1\%$ (1400 K) of carbon species, mostly HCO_3^- and CO_3^{2-} , are bonded to the stishovite surfaces, unlike in the graphene-confined solutions. In the atomic density profiles shown in Fig. 3c, d, there are oxygen and carbon density peaks near the SiO_2 surfaces, where the oxygen and carbon atoms come from the solutions, indicating that the solid-liquid interface plays an important role.

In bulk stishovite crystals, silicon atoms are octahedrally coordinated, and oxygen atoms are trigonally coordinated, whereas at the cleaved stishovite (100) surface, silicon atoms form bonds with five oxygen atoms, and each oxygen atom bridges two undercoordinated silicon atoms. Water molecules can directly bond to the stishovite surface, or dissociate under the influence of the surface. The hydroxide ion (OH^-) from water dissociation can bond to an undercoordinated silicon atom to form a silanol (Si-OH) group, and the extra proton can bond with the surface oxygen atom to become a Si-(OH $^+$)-Si bridge (Fig. 3e-g). Similar hydroxylation occurs at the quartz (1000) surface^{50,51}. In our simulations, we found reactions between hydroxyl groups at the SiO_2 surface and $CO_2(aq)$ in the solutions forming HCO_3^- . Figure 5a shows the reaction snapshots at 1000 K. The surface hydroxyl groups or the undercoordinated oxygen atoms also accept protons released in reaction (1), driving the reaction forward (Fig. 5b).

We analyzed the spatial orientation of the sp^2 carbon species such as $CO_3^{2-}(aq)$, $HCO_3^-(aq)$, and $H_2CO_3(aq)$ in the stishovite-confined solutions in Fig. 4c, d. We found that the molecular plane of the sp^2 carbon species bonded to the stishovite surface tends to form an angle of -60° or -90° with the solid-liquid interface plane, dramatically different from the orientation of carbon species in the graphene-confined solutions. When the angle is -60° , the carbon species has two Si-O bonds by straddling two silicon atoms (Fig. 4e), while with the angle

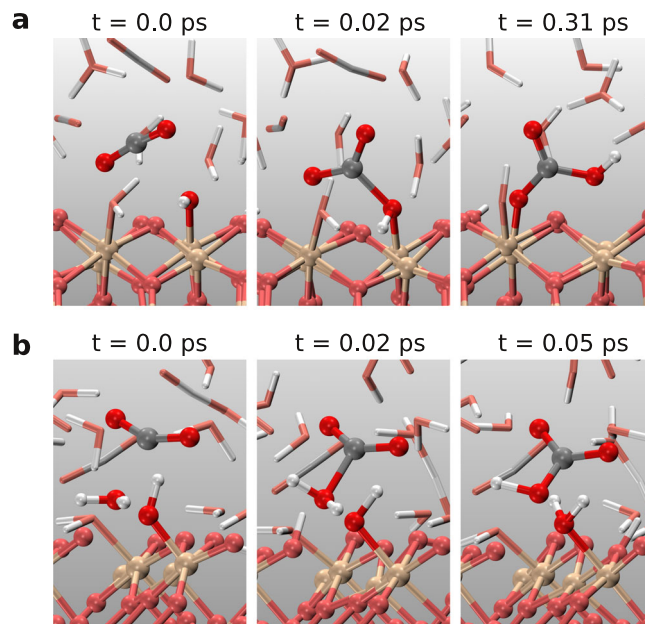


Fig. 5 | Reactions of $CO_2(aq)$ catalyzed by the stishovite (100) surface. **a** The formation of HCO_3^- at the interface. **b** The proton released from the reaction between $CO_2(aq)$ and water is accepted by the silanol (Si-OH) surface group.

of -90° the carbon species forms only one Si-O bond (Fig. 4f). The strong solid-liquid interaction substantially affects the molecular structure of the confined carbon solutions.

After analyzing the carbon species at the solid-liquid interface, we investigated the carbon species not bonded to the stishovite surface, i.e., fully dissolved in the stishovite-confined solutions. Figure 2 shows that at 1000 K, the mole percent of dissolved $CO_2(aq)$ is $10.5 \pm 2.3\%$, which is larger than $1.3 \pm 0.9\%$ in the graphene-confined solution, and slightly smaller than $15.1 \pm 2.0\%$ in the bulk solution. At 1400 K, the mole percent of dissolved $CO_2(aq)$ in the stishovite-confined solution ($39.8 \pm 3.6\%$) is also between those in the graphene-confined ($14.5 \pm 3.2\%$) and bulk ($58.8 \pm 2.0\%$) solutions.

Both hydroxide ions and protons can be chemically adsorbed on the SiO_2 surface, which affects the acidity of carbon solutions. Considering that the pH value of neutral water is no longer 7 under extreme P-T conditions, we calculated the difference between pH and pOH to quantify the acidity of solutions⁵²:

$$f = \text{pH} - \text{pOH} = -\log_{10} \left(\frac{[H_3O^+]}{[OH^-]} \right), \quad (2)$$

where $[H_3O^+]$ and $[OH^-]$ are the concentrations of hydronium and hydroxide ions, respectively. Because $CO_2(aq)$ reacts with water to generate H_3O^+ , the solutions studied here are all acidic, i.e., $f < 0$, as shown in Table 1. The interesting finding is that the f value of stishovite-confined solutions is more negative than that of graphene-confined solutions at the same P-T conditions, which means that the former is more acidic than the latter, even though less $CO_2(aq)$ reacts in the stishovite-confined solutions. We have discussed that the stishovite surface adsorbs the hydroxide ions and protons from solutions. In addition, our AIMD trajectories show that the SiO_2 surface favors the adsorption of OH^- over that of H^+ (see Supplementary Fig. 8); as a result, the stishovite-confined solutions are more acidic than the graphene-confined ones at the same P-T conditions. Increasing the concentration of H_3O^+ shifts the equilibrium of reaction (1) towards the left, so there is more $CO_2(aq)$ in the solutions.

The nanoconfinement enhances ϵ_{11} , which stabilized charged ions, so in both graphene- and stishovite-confined solutions, more $CO_2(aq)$

Table 1 | Acidity of aqueous carbon solutions: $f = \text{pH} - \text{pOH}$

T	Confinement	f
1000 K	Graphene	-1.24 ± 0.02
	Stishovite	-1.46 ± 0.02
1400 K	Graphene	-0.94 ± 0.05
	Stishovite	-1.13 ± 0.03

The initial mole fraction of $\text{CO}_2(\text{aq})$ is 0.185, and the pressure is -10 GPa. Uncertainties are obtained using the blocking method⁶⁸.

reacts than in the bulk solutions. However, it has been reported that ϵ_{\parallel} near the hydrophobic surface increases more than near the hydrophilic surface, because the motion of water molecules is more hindered at the hydrophilic surface²². Considering that the stishovite surface is more hydrophilic than graphene, charged ions are less stabilized, so we found more $\text{CO}_2(\text{aq})$ in the stishovite-confined solutions than in the graphene-confined solutions. This comes in addition to the reactions between SiO_2 and solvent molecules, which make the fluids more acidic and thereby lead to destabilization of HCO_3^- in favor of $\text{CO}_2(\text{aq})$. Therefore, the CO_2 concentration increase in the stishovite-confined solutions is a combined result of the hydrophilic confinement and the adsorption preference of OH^- on the stishovite (100) surface.

In our simulations, we used the semilocal Perdew-Burke-Ernzerhof (PBE) exchange-correlation (xc) functional⁵³, which was reported insufficient to describe aqueous systems at ambient conditions⁵⁴; however, our previous studies showed that PBE performed better for the equation of state and dielectric properties of water^{55,56} and the carbon speciation in water⁷ at extreme P-T conditions than at ambient conditions. Particularly, we compared the simulations using PBE and a hybrid xc functional, PBE0⁵⁷. For an aqueous carbon solution at -11 GPa and 1000 K, whose initial mole fraction of $\text{CO}_2(\text{aq})$ is 0.016, both PBE and PBE0 suggest that HCO_3^- is the dominant carbon species, and its mole percents are 79.8% and 75.0%, respectively⁷. Both PBE and PBE0 lack van der Waals (vdW) interactions, so we performed an additional simulation using the RPBE xc functional⁵⁸ with Grimme's D3 vdW corrections and the Becke-Johnson damping (RPBE-D3)⁵⁹. For the solution confined by graphene at 10 GPa and 1000 K, we found that the mole percents of carbon species change by <6% (see Supplementary Fig. 4 and Supplementary Table IV). Particularly, the RPBE-D3 simulation gives that the concentration of $\text{CO}_2(\text{aq})$ is 0%, while it is $1.3 \pm 0.9\%$ at the PBE level, indicating that our main conclusion that nanoconfinement enhances reactivity of CO_2 is not affected by the neglect of the vdW corrections. VdW interactions do not play a major role in breaking and forming of covalent bonds, so do not much affect the chemical speciation studied here.

In summary, we performed extensively long AIMD simulations to study the chemical reactions and speciation of aqueous carbon solutions nanoconfined by graphene and stishovite at 10 GPa and 1000–1400 K. We found that the graphene nanoconfinement promotes the $\text{CO}_2(\text{aq})$ reactions. When graphene is replaced by stishovite, less $\text{CO}_2(\text{aq})$ reacts, but still more than in the bulk solutions. We found that contacting the stishovite (100) surface makes the solutions more acidic, which shifts the chemical equilibria, though the stishovite surface also catalyzes the $\text{CO}_2(\text{aq})$ reactions by adsorbing HCO_3^- and H^+ .

The enhanced reactivity of $\text{CO}_2(\text{aq})$ in nanoconfinement has important implications for carbon transport and fluid-rock interactions in deep Earth. Aqueous fluids located at grain boundaries in minerals can either exist in isolated fluid-filled pores, or form a connected network of channels along grains facilitating fluid transport¹³. It is known that adding molecular $\text{CO}_2(\text{aq})$ to water increases the rock-fluid-rock dihedral angle θ , which inhibits fluid flow^{60,61}. However, our study shows that $\text{CO}_2(\text{aq})$ reacts with water under nanoconfinement and also reacts with the solid interface, which may decrease θ and promote the interconnectivity of fluids¹⁴. Our study also sheds light on

atomistic mechanisms of CO_2 storage through mineral carbonation. CO_2 reacts more in nanoconfined water, which benefits CO_2 mineralization. If we choose minerals with larger points of zero charge than that of SiO_2 , such as forsterite⁶² and magnesium oxide⁶³, the CO_2 reactivity may be further enhanced.

Methods

We carried out Born-Oppenheimer ab initio molecular dynamics using the Qbox package⁶⁴. We used periodic boundary conditions and employed plane-wave basis sets and norm-conserving pseudopotentials^{65,66}, with a plane-wave cutoff of 85 Ry. The cutoff was increased to 145 Ry for pressure calculations. We applied density functional theory and the PBE exchange-correlation functional⁵³. We sampled the Brillouin zone at the Γ point. We performed AIMD simulations in the canonical, i.e., NVT, ensemble. Stochastic velocity rescaling was used to control the temperature⁶⁷, with a damping factor of 24.2 fs. We replaced hydrogen by deuterium to use a large time step of 0.24 fs in the simulations, but still referred to these atoms as hydrogen atoms.

We ran simulations for 180–480 ps after 20 ps equilibration to reach chemical equilibria (see Supplementary Table I for the simulation details). We analyzed the AIMD trajectories to determine the nature of carbon-containing molecules. For each carbon atom, we searched for the three nearest oxygen atoms, and sorted the C-O distances in increasing order. If the difference between the third and second C-O distance is $<0.4 \text{ \AA}$, the carbon species is a CO_3^{2-} ion; otherwise, it is CO_2 . Hydrogen atoms were considered being bonded to their nearest-neighbor oxygen atoms. For the solutions confined by stishovite, the oxygen atoms were considered bonded to silicon atoms when the interatomic distance fell within the first peak of the Si-O_{aq} radial distribution function (RDF), i.e., 2.6 \AA , as shown in Supplementary Fig. 5. We also varied the cutoff distances (0.4 and 2.6 \AA) by $\pm 10\%$, and found that the changes of species concentrations are within the statistical fluctuations of our AIMD simulations (see Supplementary Tables V and VI).

Data availability

Input files and source data are provided in the repository: https://github.com/nstolte01/confined_aqueous_co2.

Code availability

Qbox is a free and open source code available at <http://qboxcode.org>.

References

1. Peacock, S. M. Fluid processes in subduction zones. *Science* **248**, 329–337 (1990).
2. Kelemen, P. B. & Manning, C. E. Reevaluating carbon fluxes in subduction zones, what goes down, mostly comes up. *Proc. Natl Acad. Sci. USA* **112**, E3997–E4006 (2015).
3. Manning, C. E. & Frezzotti, M. L. Subduction-zone fluids. *Elements* **16**, 395–400 (2020).
4. Zhang, C. & Duan, Z. A model for C-O-H fluid in the Earth's mantle. *Geochim. Cosmochim. Acta* **73**, 2089–2102 (2009).
5. Facq, S., Daniel, I., Montagnac, G., Cardon, H. & Sverjensky, D. A. In situ Raman study and thermodynamic model of aqueous carbonate speciation in equilibrium with aragonite under subduction zone conditions. *Geochim. Cosmochim. Acta* **132**, 375–390 (2014).
6. Sverjensky, D. A., Stagno, V. & Huang, F. Important role for organic carbon in subduction-zone fluids in the deep carbon cycle. *Nat. Geosci.* **7**, 909–913 (2014).
7. Pan, D. & Galli, G. The fate of carbon dioxide in water-rich fluids under extreme conditions. *Sci. Adv.* **2**, e1601278 (2016).
8. Abramson, E. H., Bollengier, O. & Brown, J. M. The water-carbon dioxide miscibility surface to 450 °C and 7 GPa. *Am. J. Sci.* **317**, 967–989 (2017).

9. Manning, C. E. Fluids of the lower crust: deep is different. *Annu. Rev. Earth Planet. Sci.* **46**, 67–97 (2018).
10. Stolte, N. & Pan, D. Large presence of carbonic acid in CO₂-rich aqueous fluids under Earth's mantle conditions. *J. Phys. Chem. Lett.* **10**, 5135–5141 (2019).
11. Stolte, N., Yu, J., Chen, Z., Sverjensky, D. A. & Pan, D. Water–gas shift reaction produces formate at extreme pressures and temperatures in deep earth fluids. *J. Phys. Chem. Lett.* **12**, 4292–4298 (2021).
12. Gautam, S. S., Ok, S. & Cole, D. R. Structure and dynamics of confined C–O–H fluids relevant to the subsurface: application of magnetic resonance, neutron scattering, and molecular dynamics simulations. *Front. Earth Sci.* **5**, 43 (2017).
13. Marquardt, K. & Faul, U. H. The structure and composition of olivine grain boundaries: 40 years of studies, status and current developments. *Phys. Chem. Miner.* **45**, 139–172 (2018).
14. Huang, Y., Nakatani, T., Nakamura, M. & McCammon, C. Experimental constraint on grain-scale fluid connectivity in subduction zones. *Earth Planet. Sci. Lett.* **552**, 116610 (2020).
15. Snæbjörnsdóttir, S. Ó. et al. Carbon dioxide storage through mineral carbonation. *Nat. Rev. Earth Environ.* **1**, 90–102 (2020).
16. Günther, G., Prass, J., Paris, O. & Schoen, M. Novel insights into nanopore deformation caused by capillary condensation. *Phys. Rev. Lett.* **101**, 086104 (2008).
17. Long, Y., Palmer, J. C., Coasne, B., Śliwowska-Bartkowiak, M. & Gubbins, K. E. Pressure enhancement in carbon nanopores: a major confinement effect. *Phys. Chem. Chem. Phys.* **13**, 17163–17170 (2011).
18. Hartkamp, R., Ghosh, A., Weinhart, T. & Luding, S. A study of the anisotropy of stress in a fluid confined in a nanochannel. *J. Chem. Phys.* **137**, 044711 (2012).
19. Algara-Siller, G. et al. Square ice in graphene nanocapillaries. *Nature* **519**, 443–445 (2015).
20. Chen, J., Schusteritsch, G., Pickard, C. J., Salzmann, C. G. & Michaelides, A. Two dimensional ice from first principles: structures and phase transitions. *Phys. Rev. Lett.* **116**, 025501 (2016).
21. Gao, Z., Giovambattista, N. & Sahin, O. Phase diagram of water confined by graphene. *Sci. Rep.* **8**, 6228 (2018).
22. Bonthuis, D. J., Gekle, S. & Netz, R. R. Dielectric profile of interfacial water and its effect on double-layer capacitance. *Phys. Rev. Lett.* **107**, 166102 (2011).
23. Muñoz-Santiburcio, D. & Marx, D. Nanoconfinement in slit pores enhances water self-dissociation. *Phys. Rev. Lett.* **119**, 056002 (2017).
24. Fumagalli, L. et al. Anomalously low dielectric constant of confined water. *Science* **360**, 1339–1342 (2018).
25. Ruiz-Barragan, S., Muñoz-Santiburcio, D., Körning, S. & Marx, D. Quantifying anisotropic dielectric response properties of nanoconfined water within graphene slit pores. *Phys. Chem. Chem. Phys.* **22**, 10833–10837 (2020).
26. Deißbeck, F., Freysoldt, C., Todorova, M., Neugebauer, J. & Wipperfurth, S. Dielectric properties of nanoconfined water: a canonical thermopotential approach. *Phys. Rev. Lett.* **126**, 136803 (2021).
27. Chiavazzo, E., Fasano, M., Asinari, P. & Decuzzi, P. Scaling behaviour for the water transport in nanoconfined geometries. *Nat. Commun.* **5**, 3565 (2014).
28. Thompson, W. H. Perspective: dynamics of confined liquids. *J. Chem. Phys.* **149**, 170901 (2018).
29. Phan, A. & Striolo, A. Evidence of facilitated transport in crowded nanopores. *J. Phys. Chem. Lett.* **11**, 1814–1821 (2020).
30. Muñoz-Santiburcio, D. & Marx, D. Confinement-controlled aqueous chemistry within nanometric slit pores. *Chem. Rev.* **121**, 6293–6320 (2021).
31. Turner, C. H., Johnson, J. K. & Gubbins, K. E. Effect of confinement on chemical reaction equilibria: The reactions $2\text{NO} \rightleftharpoons (\text{NO})_2$ and $\text{N}_2 + 3\text{H}_2 \rightleftharpoons 2\text{NH}_3$ in carbon micropores. *J. Chem. Phys.* **114**, 1851–1859 (2001).
32. Santiso, E. E. et al. Adsorption and catalysis: The effect of confinement on chemical reactions. *Appl. Surf. Sci.* **252**, 766–777 (2005).
33. Muñoz-Santiburcio, D. & Marx, D. Chemistry in nanoconfined water. *Chem. Sci.* **8**, 3444–3452 (2017).
34. Phan, A., Cole, D. R. & Striolo, A. Preferential adsorption from liquid water-ethanol mixtures in alumina pores. *Langmuir* **30**, 8066–8077 (2014).
35. Le, T., Striolo, A., Turner, C. H. & Cole, D. R. Confinement effects on carbon dioxide methanation: a novel mechanism for abiotic methane formation. *Sci. Rep.* **7**, 9021 (2017).
36. Miller, Q. R. S. et al. Anomalously low activation energy of nanoconfined MgCO₃ precipitation. *Chem. Commun.* **55**, 6835–6837 (2019).
37. Cole, D. R., Chialvo, A. A., Rother, G., Vlcek, L. & Cummings, P. T. Supercritical fluid behavior at nanoscale interfaces: implications for CO₂ sequestration in geologic formations. *Philos. Mag.* **90**, 2339–2363 (2010).
38. Car, R. & Parrinello, M. Unified approach for molecular dynamics and density-functional theory. *Phys. Rev. Lett.* **55**, 2471–2474 (1985).
39. Galli, G. & Parrinello, M. In *Computer Simulation in Materials Science*, (eds Meyer, M. & Pontikis, V.) 283–304 (Springer, 1991).
40. Marx, D. & Hutter, J. *Ab Initio Molecular Dynamics: Basic Theory and Advanced Methods* (Cambridge University Press, 2009).
41. Gygi, F. & Galli, G. Ab initio simulation in extreme conditions. *Mater. Today* **8**, 26–32 (2005).
42. Brandenburg, J. G. et al. Physisorption of water on graphene: Subchemical accuracy from many-body electronic structure methods. *J. Phys. Chem. Lett.* **10**, 358–368 (2019).
43. Takeuchi, K. et al. Adsorption of CO₂ on graphene: a combined TPD, XPS, and vdW-DF study. *J. Phys. Chem. C* **121**, 2807–2814 (2017).
44. Duan, Z. & Zhang, Z. Equation of state of the H₂O, CO₂, and H₂O–CO₂ systems up to 10 GPa and 2573.15 K: Molecular dynamics simulations with ab initio potential surface. *Geochim. Cosmochim. Acta* **70**, 2311–2324 (2006).
45. Akaogi, M., Yusa, H., Shiraiishi, K. & Suzuki, T. Thermodynamic properties of α -quartz, coesite, and stishovite and equilibrium phase relations at high pressures and high temperatures. *J. Geophys. Res. Solid Earth* **100**, 22337–22347 (1995).
46. Zhang, J., Li, B., Utsumi, W. & Liebermann, R. C. In situ X-ray observations of the coesite-stishovite transition: Reversed phase boundary and kinetics. *Phys. Chem. Miner.* **23**, 1–10 (1996).
47. Aoki, I. & Takahashi, E. Density of MORB eclogite in the upper mantle. *Phys. Earth Planet. Inter.* **143–144**, 129–143 (2004).
48. Lin, Y., Hu, Q., Meng, Y., Walter, M. & Mao, H.-K. Evidence for the stability of ultrahydrous stishovite in Earth's lower mantle. *Proc. Natl Acad. Sci. USA* **117**, 184–189 (2020).
49. Feya, O. D. et al. Tetrahedral honeycomb surface reconstructions of quartz, cristobalite and stishovite. *Sci. Rep.* **8**, 11947 (2018).
50. Adeagbo, W. A., Doltsinis, N. L., Klevakina, K. & Renner, J. Transport processes at α -quartz-water interfaces: Insights from first-principles molecular dynamics simulations. *ChemPhysChem* **9**, 994–1002 (2008).
51. Ledyastuti, M., Liang, Y. & Matsuoka, T. The first-principles molecular dynamics study of quartz-water interface. *Int. J. Quantum Chem.* **113**, 401–412 (2013).
52. Dettori, R. & Donadio, D. Carbon dioxide, bicarbonate and carbonate ions in aqueous solutions under deep Earth conditions. *Phys. Chem. Chem. Phys.* **22**, 10717–10725 (2020).
53. Perdew, J. P., Burke, K. & Ernzerhof, M. Generalized gradient approximation made simple. *Phys. Rev. Lett.* **77**, 3865–3868 (1996).
54. Gillan, M. J., Alfè, D. & Michaelides, A. Perspective: how good is DFT for water? *J. Chem. Phys.* **144**, 130901 (2016).

55. Pan, D., Spanu, L., Harrison, B., Sverjensky, D. A. & Galli, G. Dielectric properties of water under extreme conditions and transport of carbonates in the deep Earth. *Proc. Natl Acad. Sci. USA* **110**, 6646–6650 (2013).
56. Pan, D., Wan, Q. & Galli, G. The refractive index and electronic gap of water and ice increase with increasing pressure. *Nat. Commun.* **5**, 3919 (2014).
57. Adamo, C. & Barone, V. Toward reliable density functional methods without adjustable parameters: the PBE0 model. *J. Chem. Phys.* **110**, 6158–6170 (1999).
58. Hammer, B., Hansen, L. B. & Nørskov, J. K. Improved adsorption energetics within density-functional theory using revised Perdew-Burke-Ernzerhof functionals. *Phys. Rev. B* **59**, 7413–7421 (1999).
59. Grimme, S., Antony, J., Ehrlich, S. & Krieg, H. A consistent and accurate ab initio parametrization of density functional dispersion correction (DFT-D) for the 94 elements H-Pu. *J. Chem. Phys.* **132**, 154104 (2010).
60. Watson, E. B. & Brenan, J. M. Fluids in the lithosphere, 1. Experimentally-determined wetting characteristics of CO₂-H₂O fluids and their implications for fluid transport, host-rock physical properties, and fluid inclusion formation. *Earth Planet. Sci. Lett.* **85**, 497–515 (1987).
61. Holness, M. B. Equilibrium dihedral angles in the system quartz-CO₂-H₂O-NaCl at 800 °C and 1–15 kbar: the effects of pressure and fluid composition on the permeability of quartzites. *Earth Planet. Sci. Lett.* **114**, 171–184 (1992).
62. Wogelius, R. A. & Walther, J. V. Olivine dissolution at 25 °C: effects of pH, CO₂, and organic acids. *Geochim. Cosmochim. Acta* **55**, 943–954 (1991).
63. Kosmulski, M. Isoelectric points and points of zero charge of metal (hydr)oxides: 50 years after Parks' review. *Adv. Colloid Interface Sci.* **238**, 1–61 (2016).
64. Gygi, F. Architecture of Qbox: a scalable first-principles molecular dynamics code. *IBM J. Res. Dev.* **52**, 137–144 (2008).
65. Hamann, D. R., Schlüter, M. & Chiang, C. Norm-conserving pseudopotentials. *Phys. Rev. Lett.* **43**, 1494–1497 (1979).
66. Vanderbilt, D. Optimally smooth norm-conserving pseudopotentials. *Phys. Rev. B* **32**, 8412–8415 (1985).
67. Bussi, G., Donadio, D. & Parrinello, M. Canonical sampling through velocity rescaling. *J. Chem. Phys.* **126**, 014101 (2007).
68. Flyvbjerg, H. & Petersen, H. G. Error estimates on averages of correlated data. *J. Chem. Phys.* **91**, 461–466 (1989).

Acknowledgements

N.S. acknowledges the Hong Kong Ph.D. Fellowship Scheme. D.P. acknowledges support from the Croucher Foundation through the Croucher Innovation Award, Hong Kong Research Grants Council (Projects GRF-16307618, GRF-16306621, and C6021-19EF), National Natural Science Foundation of China (Project 11774072 and Excellent Young

Scientists Fund), the Alfred P. Sloan Foundation through the Deep Carbon Observatory, and the Hetao Shenzhen/Hong Kong Innovation and Technology Cooperation (HZQB-KCZYB-2020083). Part of this work was carried out using computational resources from the National Super-computer Center in Guangzhou, China.

Author contributions

D.P. and N.S. designed the research. Calculations were performed by N.S. R.H. implemented the van der Waals dispersion corrections into the Qbox code. N.S. and D.P. contributed to the analysis and discussion of the data and the writing of the manuscript.

Competing interests

The authors declare no competing interests.

Additional information

Supplementary information The online version contains supplementary material available at <https://doi.org/10.1038/s41467-022-33696-w>.

Correspondence and requests for materials should be addressed to Ding Pan.

Peer review information *Nature Communications* thanks Riccardo Dettoni, and the other, anonymous, reviewer(s) for their contribution to the peer review of this work. Peer reviewer reports are available.

Reprints and permission information is available at <http://www.nature.com/reprints>

Publisher's note Springer Nature remains neutral with regard to jurisdictional claims in published maps and institutional affiliations.

Open Access This article is licensed under a Creative Commons Attribution 4.0 International License, which permits use, sharing, adaptation, distribution and reproduction in any medium or format, as long as you give appropriate credit to the original author(s) and the source, provide a link to the Creative Commons license, and indicate if changes were made. The images or other third party material in this article are included in the article's Creative Commons license, unless indicated otherwise in a credit line to the material. If material is not included in the article's Creative Commons license and your intended use is not permitted by statutory regulation or exceeds the permitted use, you will need to obtain permission directly from the copyright holder. To view a copy of this license, visit <http://creativecommons.org/licenses/by/4.0/>.

© The Author(s) 2022